

Article

Dense, Strong, and Precise Silicon Nitride-Based Ceramic Parts by Lithography-Based Ceramic Manufacturing

Altan Alpay Altun ¹, Thomas Prochaska ¹, Thomas Konegger ² and Martin Schwentenwein ^{1,*} 

¹ Lithoz GmbH, Mollardgasse 85A/2/64-69, 1060 Vienna, Austria; aaltun@lithoz.com (A.A.A.); tprochaska@lithoz.com (T.P.)

² TU Wien, Institute of Chemical Technologies and Analytics, Getreidemarkt 9/164-CT, 1060 Vienna, Austria; thomas.konegger@tuwien.ac.at

* Correspondence: mschwentenwein@lithoz.com; Tel.: +43-1-934-661-2204

Received: 27 December 2019; Accepted: 25 January 2020; Published: 3 February 2020



Abstract: Due to the high level of light absorption and light scattering of dark colored powders connected with the high refractive indices of ceramic particles, the majority of ceramics studied via stereolithography (SLA) have been light in color, including ceramics such as alumina, zirconia and tricalcium phosphate. This article focuses on a lithography-based ceramic manufacturing (LCM) method for β -SiAlON ceramics that are derived from silicon nitride and have excellent material properties for high temperature applications. This study demonstrates the general feasibility of manufacturing of silicon nitride-based ceramic parts by LCM for the first time and combines the advantages of SLA, such as the achievable complexity and low surface roughness ($R_a = 0.50 \mu\text{m}$), with the typical properties of conventionally manufactured silicon nitride-based ceramics, such as high relative density (99.8%), biaxial strength ($\sigma_f = 764 \text{ MPa}$), and hardness ($\text{HV}_{10} = 1500$).

Keywords: additive manufacturing; silicon nitride; high performance ceramics; photopolymerisation; lithography-based ceramic manufacturing

1. Introduction

The history of silicon nitride (Si_3N_4) ceramics began about 150 years ago, with Deville and Wöhler developing silicon nitride synthetically in 1857 [1], even though naturally occurring nierite minerals, such as α - Si_3N_4 and β - Si_3N_4 , have been found during later, detailed analyses of particles of meteoritic rock [2]. Silicon nitride currently plays a dominant role in the field of nonoxide ceramics, and exhibits a combination of excellent material properties, such as high toughness and strength at high temperatures, excellent thermal shock resistance and good chemical resistance, which is unmatched by other ceramics [3]. Due to these superior material properties, silicon nitride ceramics became popular in the 1950s, e.g., for use in thermocouple tubing [4]. Owing to these properties, in particular thermal conductivity and thermal and corrosion resistance, silicon nitride-based ceramics can also be used as base material for thermal conductors, gas turbines, and ball bearings [5]. Apart from technical applications silicon nitride-based ceramics have also been used as material for medical devices (e.g., spinal cages). It was shown that the material shows good osseointegration and stimulated cell differentiation as well as osteoblastic activity which resulted in accelerated bone ingrowths compared to poly (ether ether ketone) (PEEK) [6]. Furthermore, silicon nitride was also evaluated regarding its anti-infective behavior when used for implants. Webster et al. compared the bacterial growth on calvarial implants in rats of silicon nitride to implants made of either titanium or PEEK [7]. They observed bacteria in 88% of the PEEK implants and 12% of the titanium implants whereas no bacteria

were present adjacent to the silicon nitride implants. Similar results have also been observed by Ishikawa et al. in tibial implants [8]. These properties, together with its excellent biocompatibility and mechanical strength, make silicon nitride to a very attractive material for biomedical engineering [9]. The combination of load-bearing ability and induction of cell differentiation makes it superior to classical bone replacement materials like calcium phosphates. Additionally, the bactericidal behavior could drastically reduce infection associated implant failures or necessary revision surgeries, which have quadrupled in the last 20 years [10].

The solid phase sintering of pure silicon nitride ceramics is generally not feasible due to decomposition processes and low diffusion coefficients. Based on that reasoning, sintering additives are needed to allow for consolidation by sintering. The first sintering aid investigated for the densification of Si_3N_4 ceramics was magnesium oxide (MgO). Subsequently, other materials such as alumina (Al_2O_3), yttria (Y_2O_3), zirconia (ZrO_2) and ceria (CeO_2) were used to further promote densification. Overall, the yttria–alumina (Y_2O_3 - Al_2O_3) system is the most widely applied sintering aid system [11]. An effective method for increasing the creep and oxidation resistance of silicon nitride is the addition of large amounts of sintering additives to the silicon nitride structure in the grain boundary phase, the formed mixed crystals being known as SiAlONs [12,13]. SiAlON ceramics are the solid solution of silicon nitride and the sintering additives alumina (Al_2O_3), yttria (Y_2O_3) and aluminum nitride (AlN). In the early 1970s, the formation of this solid solution that has the same structural form as silicon nitride has been reported in Japan and in the UK parallel [14]. Since the SiAlON powders contain the sintering aids, the sintering additives were not blended additionally in this work.

Conventional methods for manufacturing intricate ceramic bodies demand difficult and costly production steps. As a result, the manufacturing industry becomes less interested in creating highly complex geometries due to the high price of the molds, the extended production times, and the challenging consolidation behavior. However, with the introduction of additive manufacturing (AM), there was new potential to create elaborate shapes which had been impossible to achieve using conventional techniques. AM refers to a class of technologies in which a three dimensional (3D) object is manufactured directly from a computer aided design (CAD) model. It is defined by ASTM F2792—12a (Standard Terminology for Additive Technologies) as “the process of joining materials to make objects from 3D model data, usually layer upon layer, as opposed to subtractive manufacturing, such as traditional machining” [15].

Ceramic AM technologies can be divided into two groups: direct and indirect methods [16]. Typical steps involved in indirect methods include casting of ceramic suspension into a temporary mold, which is fabricated via conventional 3D printing (3DP), followed by the subsequent solidifying and sintering process. The main advantages of indirect methods of AM are the absence of delamination processes and the isotropy of characteristics; however, problems arise when discarding the mold, creating a possible dilemma when using indirect methods. Direct methods, on the other hand, allow for more freedom in terms of complexity, and have less processing steps due to the fabrication of ceramic materials, layer-by-layer, directly onto the building platform. Depending on the raw materials, direct methods can also be divided into powder-, suspension-, precursor-, melting-, and reaction-based processes. Powder-based processes, such as binder-jet 3DP and selective laser melting (powder bed fusion), use ceramic particles in a powder bed to build 3D objects. The advantage of powder bed fusion is the possibility to manufacture ceramics parts without requiring any subsequent sintering process, however, the fabricated parts can be porous and the thermal distortion can cause warping of fabricated objects [17–19]. In the suspension-based processes, ceramic powders are formed with the aid of a matrix of monomers, polymers, photopolymers, or solvents. Stereolithography (SLA), laminated object manufacturing (LOM), robocasting and fused filament fabrication (FFF) are the typical examples of processes depending on the type of binder [20–23]. The process is completed by removing the organic components through evaporation or decomposition and subsequent densification by sintering.

Among these techniques, SLA is still the most prominent AM method due to the high resolution of the surface, facilitating the production of an increasing number of different types of materials.

Precursor-based processes rely on the conversion of inorganic polymers into ceramics through pyrolysis. The limited thickness of these materials due to the extremely high volume loss during the pyrolysis step is the main challenges here [24]. Melting-based processes can only be used with low melting point ceramics such as glass. Melted glass is deposited through a nozzle and then cooled to room temperature in order to obtain transparent materials with superior material properties [25]. Reaction-based processes (e.g. plaster-based 3D inkjet printing), in contrast, generally require thermal post-processing treatment to obtain the desired final materials. Recently a modified technique has been reported involving a chemical reaction of ceramic particles with an ink to fabricate ceramic bodies without requiring any further thermal post-processing treatments such as sintering [16].

Lithography-Based Ceramic Manufacturing Process

Lithography-based techniques are based upon the concept of photopolymerisation. The lithography-based ceramic manufacturing process has been developed for highly filled and highly viscous ceramic suspension. Figure 1 shows the schematic system of the LCM process. A photosensitive formulation is cured in the required areas through selective light exposure to light. In the case of lithography-based ceramic manufacturing (LCM), the suspension is cured via a mask-exposure process using the concept of digital light processing (DLP). The optics used currently generate a pixel size of $40 \times 40 \mu\text{m}$ with a resolution of 1920×1080 pixels.

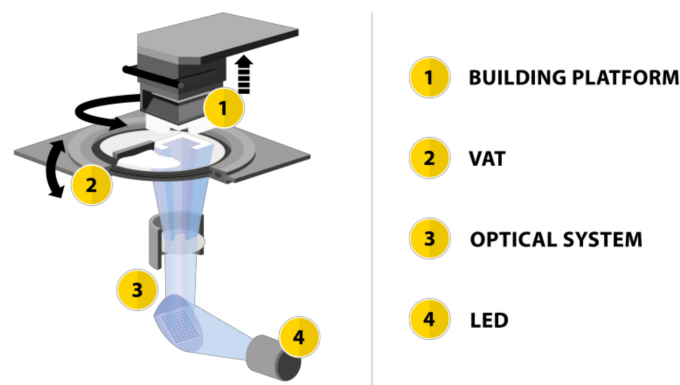


Figure 1. Schematic drawing of the Lithography-based Ceramic Manufacturing (LCM) process: (1) building platform; (2) vat; (3) optical system; (4) light engine.

Once the three-dimensional structure is shaped, the part is called a green body, in which the ceramic particles are now surrounded by a polymer network; however, the photopolymer only acts as a binder in the ceramic green body [26]. For this reason, this composite material requires additional thermal treatment through the processes of debinding and sintering. During the debinding step, the polymer network is burned off and the subsequent sintering step causes densification by fusing the ceramic particles together.

The LCM process is carried out using a printer composed of a building platform, a vat, an optical system and a light engine (Figure 1). First, the vat is filled with the photocurable ceramic suspension and the building platform then begins to move down into the suspension until the gap between the building platform and the vat is a chosen distance, typically between 10 and 100 μm . This gap, corresponding to the resulting thickness of the printed layer of the green body, is chosen according to the optical properties and photoreactivity of the ceramic suspension as well as the needed resolution of the printed part. Then, the photocurable suspension is cured selectively through a mask-exposure process from the bottom of the transparent vat. The light engine is based on light-emitting diodes (LED) with a wavelength of 460 nm. By repeating this process layer for layer, the green body is manufactured.

After printing of the green body, the LCM process also involves a thermal treatment which comprises debinding (removal of binder) and sintering (densification of ceramics), comparable to conventional techniques (see Figure 2) [26]. The removal of organic components is the most critical

step in the process. For this reason, a reduction of binder concentration or a high solids loading of ceramic particles is desired. During the debinding, the photocured binder is burned off, typically under air atmosphere. Due to the evaporation or decomposition behavior of organic components at different temperatures, a tailored temperature profile has to be used to obtain crack-free ceramics after thermal post processing [27]. Here, thermogravimetric analysis and differential scanning calorimeter are suitable tools to select adequate parameters. In contrast to oxide ceramics, nonoxide ceramics, such as silicon nitride and silicon carbide, need an inert atmosphere during sintering step in order to avoid oxidation. The interaction between ceramics particles at high temperatures induces densification via sintering and, consequently, fully dense ceramics are formed [28,29].

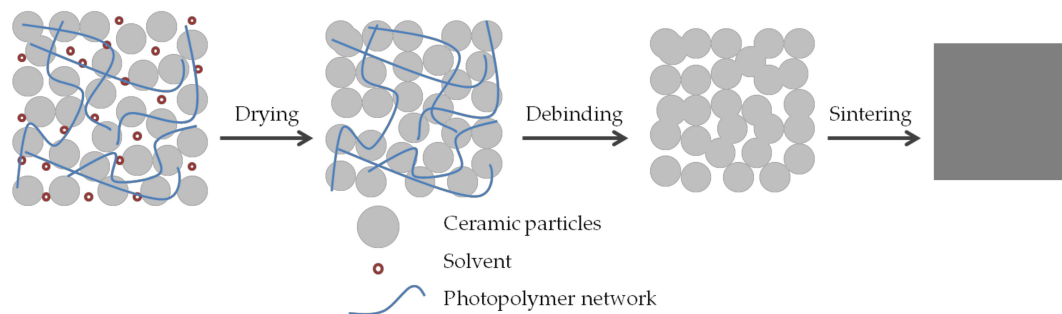


Figure 2. Steps of the thermal treatment after green body fabrication: drying, debinding and sintering.

LCM has been demonstrated to be highly capable when it comes to the precision and mechanical properties of the fabricated parts and has already been successfully applied to fabricate complex-shaped ceramics from alumina, yttria-stabilized zirconia, tricalcium phosphate, mullite, silicon oxycarbide and magnesia [30–35].

In this work, we report on the development of an LCM process for the production of highly complex-shaped silicon nitride-based ceramics exhibiting mechanical properties at the same level of conventionally manufactured materials. As processing of silicon nitride powders by stereolithographic methods is highly challenging, both during the AM stage and during the consolidation stage, this has to our knowledge not been achieved previously, our study thus being the first of its kind. Chung et al. have published that the silicon nitride-based green bodies could be printed by digital light processing; however, the sintered silicon nitride-based ceramics have a relative density of approximately 90% which is significantly lower than the results obtained within this work [36]. In addition to this, the published article has a lack of some analyses such as surface roughness of printed samples, stability of the ceramic suspension, thermogravimetric analysis of the ceramic suspension. According to the photos from Chung' work, the resolution and complexity of the printed samples are also incomparably lower than the results obtained within this work.

2. Materials and Methods

2.1. Suspension Characterization

In the LCM process, the layer thickness is one of the crucial parameters for the shaping process. For this reason, light penetration tests were conducted to quantify how far light can penetrate into a given ceramic suspension. The ceramic suspension was exposed to the same level of maximum light intensity (47.1 mW cm^{-2}) for five different time periods, resulting in distinct energy doses through a cylinder with a diameter of 10 mm. The number of tested suspension samples was 3 for each of the energy doses. The thickness of the polymerized layer was then measured using a micrometer screw. Once the thickness of the polymerized layer was determined, the lateral over-polymerization was also measured for all polymerized layer with an aid of a light microscope. The difference between target value and actual value was noted as over-polymerization. Griffith et al. have shown that the

scattering efficiency term (Q) is proportional to the difference of refractive indices (n) between the ceramic particles and photocurable matrix.

$$Q = \beta \Delta n^2 \quad (1)$$

$$\Delta n^2 = (n_{\text{ceramic}} - n_{\text{solution}})^2 \quad (2)$$

The penetration depth is inversely proportional to the refractive index, and the term β is relevant to the particle sizes and wavelengths [26]. The refractive index of silicon nitride powder is 2.0167 [37], whereas the refractive index of organic binder is 1.4630 (± 0.0005).

The rheological measurements of photocurable suspension were performed on a rheometer (MCR 92, Anton Paar, Graz, Austria) at a temperature of 20 °C with a plate–plate arrangement. The plate–plate measuring system has a diameter of 25 mm and the gap between plates was 0.5 mm. The viscosity was measured three times for each linearly at shear rates between 5 and 50 s⁻¹.

Finally, an evaluation of the typical materials efficiency was performed for the LCM process in combination with the LithaNit 720 suspension that was employed in this work. For this reason, the weight of the suspension was recorded both before and after printing. Furthermore, the exact mass of printed samples in the green state was measured once the parts had been cleaned. The factor of suspension was calculated by dividing the mass of the suspension for printing by the mass of the printed parts after cleaning is a measure for the materials efficiency of the used LCM process. This process was repeated three times in order to find a mean value and standard deviation.

2.2. Sample Preparation

In this study, the silicon nitride-based ceramic parts were manufactured using a commercially available photocurable ceramic suspension LithaNit 720 (Lithoz GmbH, Vienna, Austria), which has a solid loading of 40 vol. %. LithaNit 720 consists of a SiAlON powder blend and a photocurable binder system.

After printing and cleaning of the samples, debinding was conducted in an air furnace (HTCT 08/16, Nabertherm, Lilienthal, Germany), using a temperature profile as shown in Figure 3. Subsequently, the debinded samples were transferred to the sintering furnace. Sintering was performed at 1750 °C with a dwelling time of 5 hours under nitrogen atmosphere using a graphite-heated furnace (KCE HP W 150/200-2200-100 LA). During sintering, the samples were embedded in a powder bed consisting of a mixture of silicon nitride and boron nitride as sintering aids to ensure the separation of the sintered ceramic parts and crucibles.

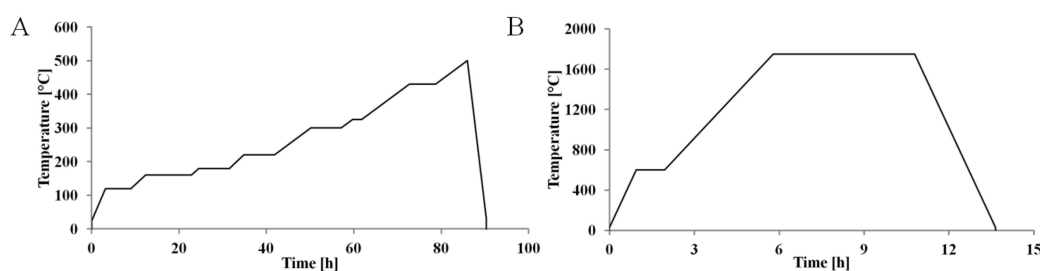


Figure 3. Complex temperature profile of silicon nitride-based green bodies: (a) debinding (b) sintering.

2.3. Sample Characterization

Thermogravimetric analysis (TGA 2050; TA Instruments, New Castle, USA) was performed to quantify the mass loss during a thermal treatment as a function of temperature, using a cylindrical sample with both a diameter and height of 6 mm. The specimen was heated from room temperature to 500 °C at a rate of 2 K/min in nitrogen atmosphere and air.

The surface roughness of the printed silicon nitride-based ceramics was analyzed by tactile profilometry using a SurfTest SJ-400 Profilometer (Mitutoyo, Kanagawa, Japan) according to ISO

(International Organization for Standardization) 1997. Figure 4 depicts the orientations of the samples on the building platform of the CeraFab machine (a) and the sintered ceramic samples (b). The sintered ceramic parts have a main dimension of $14.66 \times 2.00 \times 5.54$ mm (L \times W \times H). The aim of three different orientations such as X, Y and 45° is to see the effect of the projector pixel pattern and to interpret the results statistically. As such, the assessed samples were tested post-firing without subsequent surface treatment such as grinding or polishing.

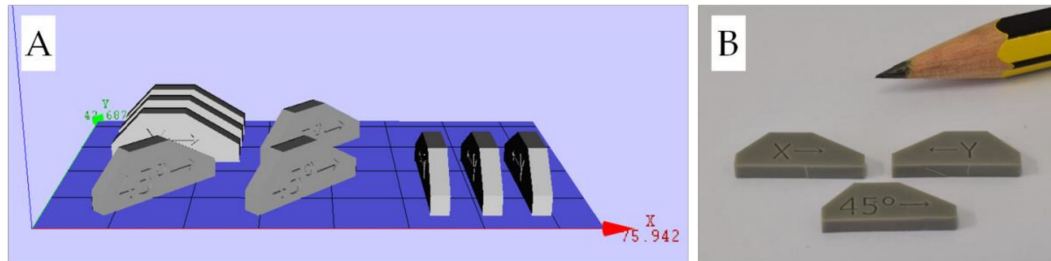


Figure 4. Samples for surface roughness measurement: (a) 3D model (b) sintered samples.

Density measurements were conducted for three cylinders with a diameter of 6 mm and a height of 10 mm, following the Archimedeian principle using a density determination kit (SI-234A, Denver Instrument, Bohemia, NY, USA), allowing for determination of relative density (assuming a theoretical density of 3.24 g cm^{-3}).

The biaxial flexural test was used to characterize the mechanical strength of the brittle silicon nitride-based ceramic samples according to ASTM (American Society for Testing and Materials) F394-78. The samples had a diameter of 22 mm and a thickness of 2.5 mm. The number of tested samples per batch was 7. Before testing the samples, the disc surfaces were polished. The tests were performed on a universal testing machine (Instron Universal, MA, USA). As shown in Figure 5a, the specimen was placed on supporting balls and the central force was applied by a fourth loading ball.

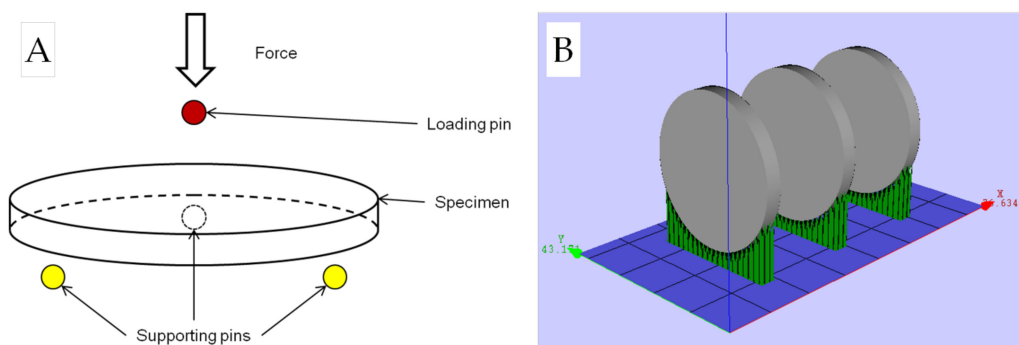


Figure 5. (a) Principle of biaxial flexural strength measurement; (b) orientation of the individual layers for biaxial flexural strength disc, including the support structure (removed prior to sintering).

AM-produced parts often exhibit anisotropic mechanical strength [38]. In this investigation, each biaxial flexural test disc was printed standing on its cylinder jacket. Thus, the orientation of the individual layers is perpendicular to the direction of the load applied during the biaxial test, as can be seen in Figure 5b. In this case, the load is applied in direction of the layer boundaries; thus, this orientation typically gives the weakest possible strength values.

The hardness of the sintered silicon nitride-based ceramics was also tested with the same sample design using a test load of 10 kgf, as according to Vickers (HV_{10}). Ekström et al. have declared that dense SiAlON materials have a hardness HV_{10} of approximately 1500 [39].

The microstructure of the sintered silicon nitride-based ceramics and their fracture surfaces were evaluated using scanning electron microscopy, SEM (Quanta 200, FEI, USA). A light microscope (Opto, Graefelfing, Germany) was used to determine the minimum wall thickness of sintered specimens.

Thermal shock resistance is an important property for high temperature applied materials. To simulate the required conditions, the printed samples were heated up to 800 °C with a dwelling time of 3 hours and a heating rate of 10 K/min. At the end of the dwelling time, the three samples (test bars with a dimension of 5 × 5 × 25 mm) were quenched in water at room temperature respectively. The thermal shock resistance test samples were evaluated using light microscopy and SEM.

The thermal conductivity (λ) was calculated from the thermal diffusivity that was measured by means of laser flash analysis (XFA 500, Gammadata Instrument AB, Uppsala, Sweden). Printed silicon nitride-based discs (\varnothing 22 mm with a thickness of 2.5 mm) were placed in a vertical setup that had a light source on the bottom side and a detector on the top side. The samples were heated up from the bottom side with an aid of laser pulse and a detector saved the temperature during time on the top side. The thickness of the three discs and the temperatures of the plates were used to calculate the thermal conductivity.

The X-Ray Diffraction (XRD) spectra were collected using a diffractometer (X'Pert Pro, PANalytical). The surface of the sample (10 × 10 × 1 mm) was polished to achieve a flat surface. The 2θ values between 5° and 100° were measured with Cu K α radiation ($\lambda = 0.154$ nm). The phases were evaluated using a Rietveld refinement with HighScore software.

3. Results

3.1. Suspension Characterization

The optimal level of energy needed to print the samples was determined via the cure depth of the photocurable suspension. The result of the cure depth test can be seen in Figure 6a. Due to the high level of absorption and scattering of light by the silicon nitride particles, the cure depth is significantly lower than that of other ceramic particles such as alumina or zirconia. The binder system, which is a light-sensitive organic matrix, is based on an acrylate-based monomer system and contains some additives, such as solvents and a photoinitiator [26,30]. According to Mitteramskogler et al., the curing depth should be approximately three times thicker than the printed layers to avoid the cracks during the thermal post-processing. Based on these results, all the parts generated in this study were printed using a CeraFab 7500 system (Lithoz GmbH, Vienna, Austria) with a layer thickness of 20 μm and an energy dose of 350 mJ cm^{-2} . In addition to the cure depth, the lateral over-polymerization was measured with an aid of a light microscope (see Figure 6b; $E = 350 \text{ mJ/cm}^2$). As it is a deviation from the target dimensions, lateral over-polymerization should be avoided in order to print precise and accurate structures [40]. Due to the pixel arrangement, lateral over-polymerization does not affect tragically in that case because in that range the surface first begins to round itself.

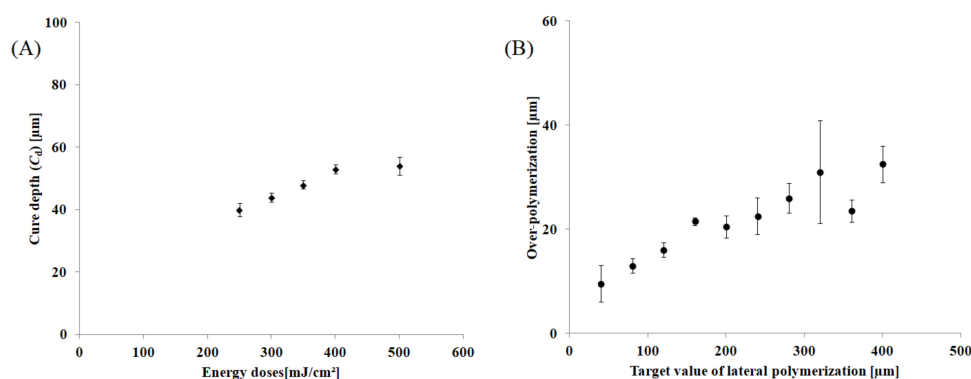


Figure 6. Cure depth (C_d) with different energy doses (a); lateral over-polymerization measurements (b) for silicon nitride-based ceramic suspension.

Figure 7 depicts the rheological behavior of the suspension at the relevant shear rates between 5 and 50 s^{-1} . Stability of the suspension was also tested by means of rheological measurements. Fresh suspension was tested (Week 0; blue dashed line) and the same suspension was also measured 8th

weeks after production, both before (Week 8; red dotted dashed line) and after (Week 8*; red solid line) re-homogenization with the aid of a centrifugal mixer. Although 8-week-old suspension has a dissimilar rheological behavior to fresh suspension, centrifugal mixing helps to achieve very similar properties to the fresh suspension and can still be printed using the very same process parameters. In addition to this, all the measured viscosities have a standard deviation of less than 0.04 Pa.s.

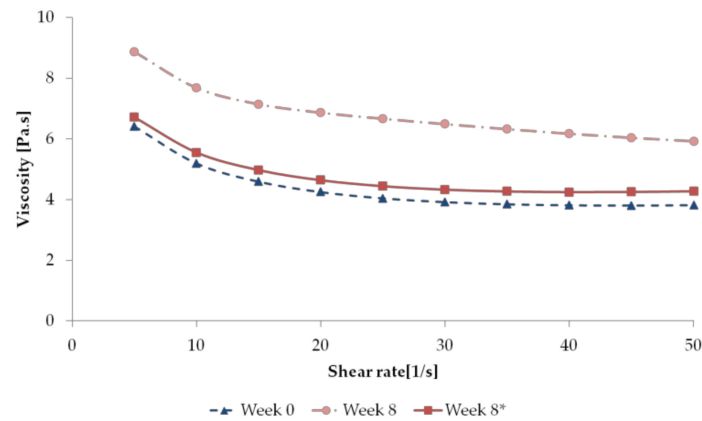


Figure 7. Viscosity of the photocurable silicon nitride-based suspension as a function of the shear rate for Week 0 and Week 8.

Finally, in terms of material efficiency, tests were performed for the three different printing cycles resulting in a variety of geometries such as test bars ($5 \times 5 \times 25$ mm) and discs (\varnothing 22 mm with a thickness of 2.5 mm). The amount of suspension, which was converted into shaped green parts was measured to be 89% of the LithaNit 720 suspension that was fed into the printer, which means that only approximately 13% of suspension was lost during the manufacturing of the samples (mainly due to cleaning of the green parts). This high material efficiency sets LCM distinctly apart from any other stereolithography process.

3.2. Sample Characterization

In order to gain insights into the debinding process and the effect of the debinding atmosphere, thermogravimetric analyses of the LithaNit 720 materials were carried out. Figure 8 depicts the mass changes of samples in air (blue dotted line) and in nitrogen (red solid line). The decomposition of the organic binder was completed at approximately 350 °C–400 °C in the air, whereas binder decomposition was shifted to 400 °C–450 °C in the nitrogen atmosphere, illustrating a difference in weight loss behavior due to oxidation processes. Total mass losses were 35.3% and 34.8%, respectively.

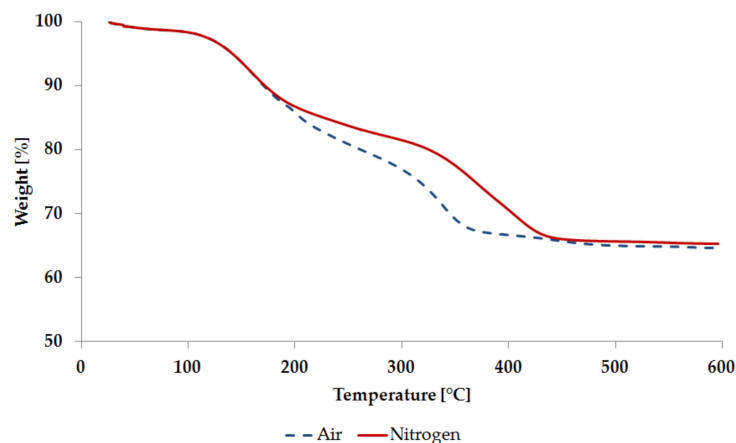


Figure 8. TGA curves for LithaNit 720 green bodies during debinding as a function of atmosphere (blue dashed line: air; red solid line: nitrogen).

The density of the sintered ceramics was determined according to the Archimedean principle by immersing in water with a measured density of 3.24 g cm^{-3} , corresponding to a relative density of 99.8 (± 0.2)% (taking into account the theoretical density reported for silicon nitride-based ceramics). These excellent densification values are comparable to conventionally produced silicon nitride-based ceramics.

Surface roughness was determined for a variety of surface orientations, as shown in Figure 9a. Measurements were performed in five different directions for three different orientated samples (namely X, Y and 45°) and the R_a values were summarized in Figure 9b. Due to the minor effect of the orientation on the building platform, the average values were noted for three different orientated samples. The average roughness R_a was $0.50 (\pm 0.03) \mu\text{m}$ along the layer boundaries (4) and $0.70 (\pm 0.04) \mu\text{m}$ perpendicular to the individual layers in the printing direction (5). The surface roughness value is a combination of the layer thickness, the angle of sample, and also the accuracy of the additive manufacturing process. Surfaces of (1) 45° , (2) top and (3) 60° show an average roughness R_a of $1.97 (\pm 0.11) \mu\text{m}$, $0.76 (\pm 0.04) \mu\text{m}$ and $2.36 (\pm 0.12) \mu\text{m}$, respectively. This can be explained by the staircase effect, which is caused by the layer-by-layer part building and also the surface angles of ceramic parts such as 45° (3) and 60° (1), resulting in a surface roughness greater than the roughness along other sample orientations [41]. However, the R_a values observed in this study are lower than values typically observed in nonlithographic AM methods [42], and are even lower than surface roughness values reported for alumina ceramics generated by LCM [30].

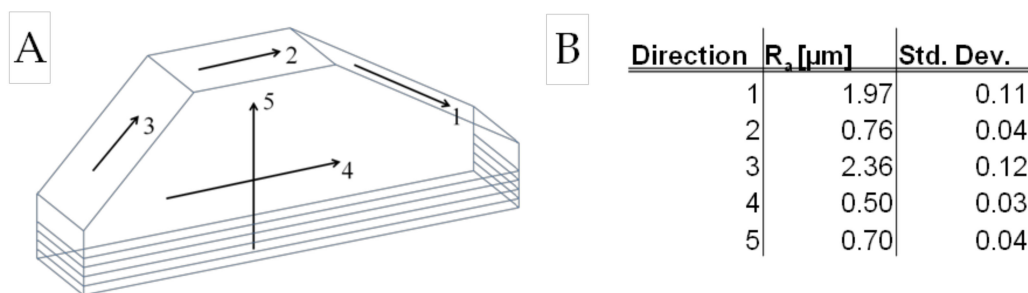


Figure 9. (a) Directions of roughness measurement; (b) summary of surface roughness of measured samples.

Due to the elimination of edge failures by multiaxial stress, the biaxial flexural strength has advantages over uniaxial bending strength. Figure 10 shows the compressive load (N) of the tested biaxial discs, which was $1011 (\pm 171) \text{ N}$. The biaxial strength was calculated as $764 (\pm 137) \text{ MPa}$. This value can be converted into a three-point bending strength of about 950 MPa , which is the same value as for conventionally manufactured iso-pressed silicon nitride-based ceramics 945 MPa [43]. Although the printing direction was the nominally weakest orientation, the mechanical properties are very similar to conventionally iso-pressed silicon nitride-based ceramics. In addition to strength, the hardness of the biaxial discs was also measured. The resulting value of $\text{HV}_{10} 1500$ is comparable to values reported for conventionally produced silicon nitride-based ceramics.

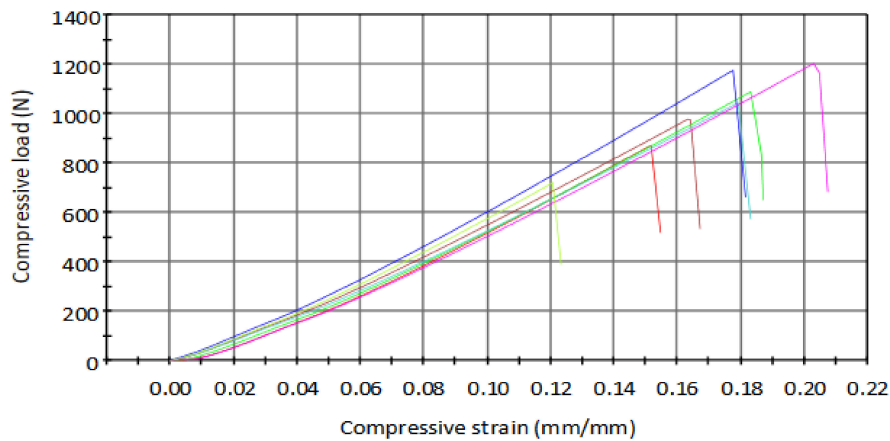


Figure 10. Biaxial flexural strength of sintered silicon nitride-based ceramics.

After determining the biaxial flexural strength and hardness of the sintered silicon nitride-based ceramic discs, fracture surfaces of the disc samples were investigated via SEM. Figure 11 depicts the fractography of samples in different magnifications. No residual layer structures introduced during the AM process were visible. Furthermore, no microcracks were observed, resulting in a smooth fracture surface. As a result of the successful consolidation process, no residual porosity was found (see Figure 11c).

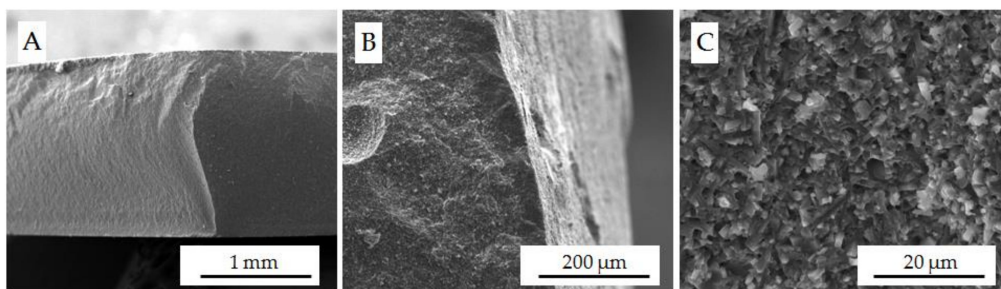


Figure 11. Scanning electron micrographs of biaxial flexural disc fracture surfaces of sintered silicon nitride-based ceramic specimens, in different magnifications with a scale bar of (a) 1 mm; (b) 200 μm ; (c) 20 μm .

In order to inspect the minimum wall thickness, a highly macroporous gyroid-type design was printed. Figure 12 illustrates that sintered silicon nitride-based ceramics can be manufactured with a wall thickness of 265 μm without visible crack formation. The scaffold designs with a wall thickness up to 100–300 μm are commonly used for biomedical investigations [44]. For that reason, studies towards further reduction of minimum wall thickness to well below 200 μm are currently underway.

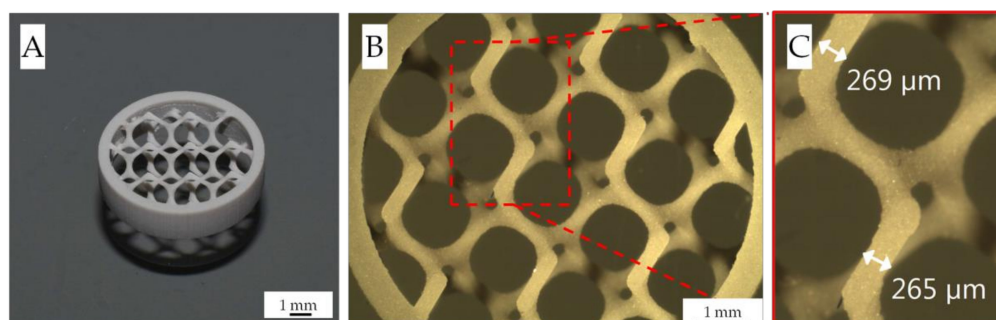


Figure 12. Printed and sintered silicon nitride-based ceramics using the LithaNit 720 suspension: (a) gyroids design, (b) and (c) light microscope images in different magnifications.

The thermal shock resistance of the silicon nitride-based ceramics generated by LCM was investigated by water quenching from 800 °C to room temperature. The microstructures of these test bars can be seen in Figure 13a (before water-quenching) and Figure 13b (after water-quenching). Despite the high thermal stress, no visible microcracks or other microstructural changes such as oxidation were observed.

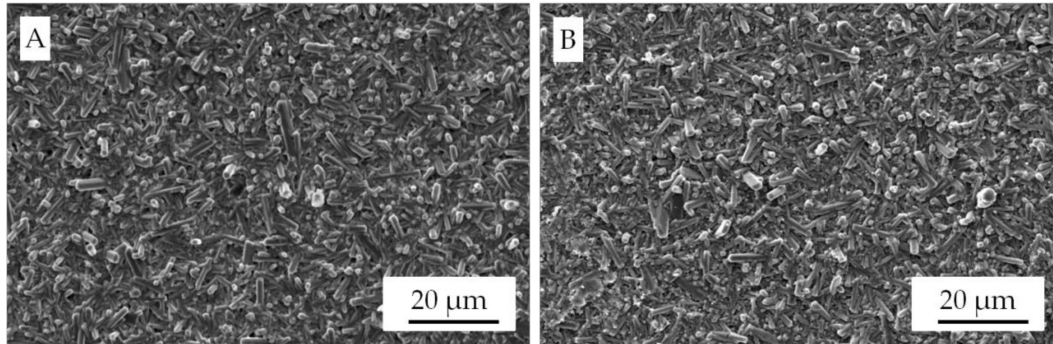


Figure 13. SEM micrographs of printed & sintered samples (a) before and (b) after thermal shock resistance test (water-quenching from 800 °C).

Thermal conductivity of conventional SiAlON grades typically varies between 20–40 $\text{Wm}^{-1}\text{K}^{-1}$ for [3,43]. The thermal conductivity of the printed silicon nitride-based ceramic parts within this study was measured as 28.2 (± 0.4) $\text{Wm}^{-1}\text{K}^{-1}$ using the laser flash method, which is a reasonable value for industrial applications, such as high frequency circuit substrates with ultimate thermal requirements.

The XRD analysis of the silicon nitride-based ceramics is shown in Figure 14. According to diffractogram by far the largest part of the sintered ceramic consists primarily of β -SiAlON. The sample also contains traces of a pure Y_2O_3 and pure Si_3N_4 . These findings are not surprising since yttria is the most prominent sintering aid responsible for the formation of the glass phase. Due to the nature of liquid phase sintering, it is possible to find traces of pure Si_3N_4 .

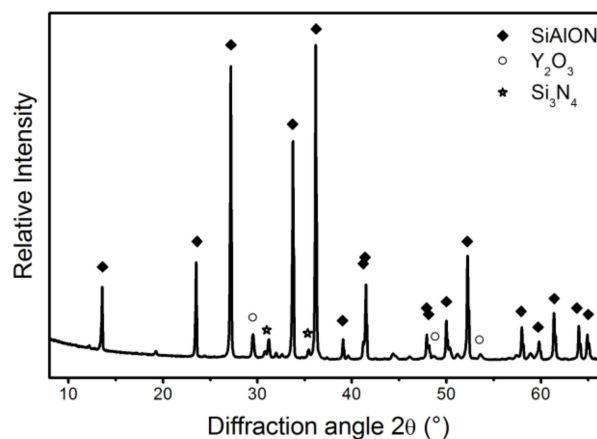


Figure 14. XRD analysis of the sintered silicon nitride-based ceramics.

4. Conclusions

In the present study, a variety of silicon nitride-based ceramic parts with complex architecture were manufactured for the first time using the lithography-based ceramic manufacturing (LCM) method, achieving material characteristics comparable to materials obtained by conventional ceramic manufacturing methods (Figure 15). After additive manufacturing using a newly developed photopolymer-containing suspension, SiAlON ceramic bodies with a relative density of 99.8% were obtained, exhibiting a biaxial strength of 764 MPa and a hardness of 1500 (HV_{10}). The advantages of LCM technology, such as the ability to fabricate highly precise and small complex ceramic

parts, have the potential to entirely innovate the shaping of nonoxide ceramic materials in general and silicon nitride-based materials in particular. This process enables the fabrication of highly complex components (such as the ones shown in Figure 15, Figure 16), which cannot be obtained by conventional processing techniques, such as insulators, springs, impeller, microturbines and cutting tools. Additionally, due to the superb biocompatibility and good osseointegration and anti-infective (bactericidal) properties, silicon nitride makes a perfect candidate for dental (Figure 16b), orthopedic (Figure 16e) and craniomaxillofacial implants.

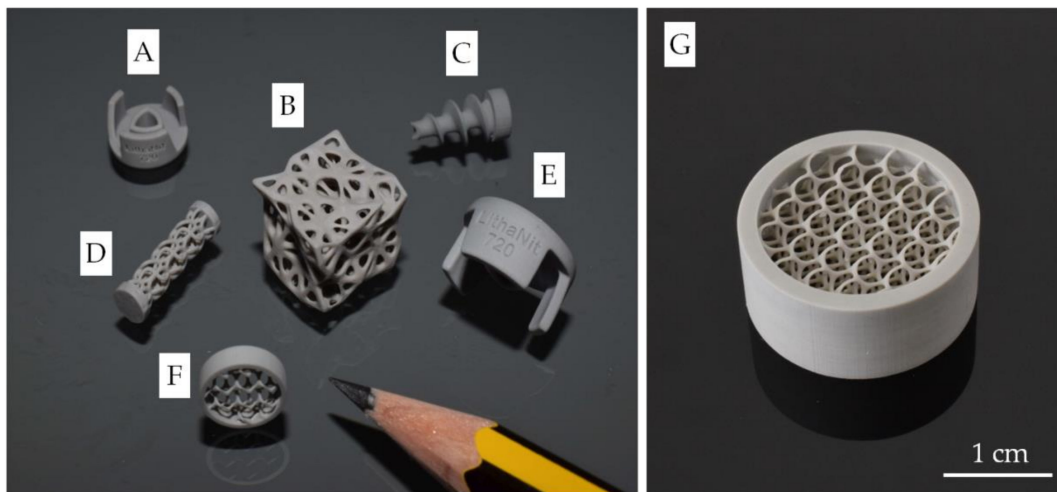


Figure 15. Printed and sintered silicon nitride-based ceramic demonstrators: insulator (a) and (e), dummy design (b), screw (c), spring (d), cellular designs (f) and (g).

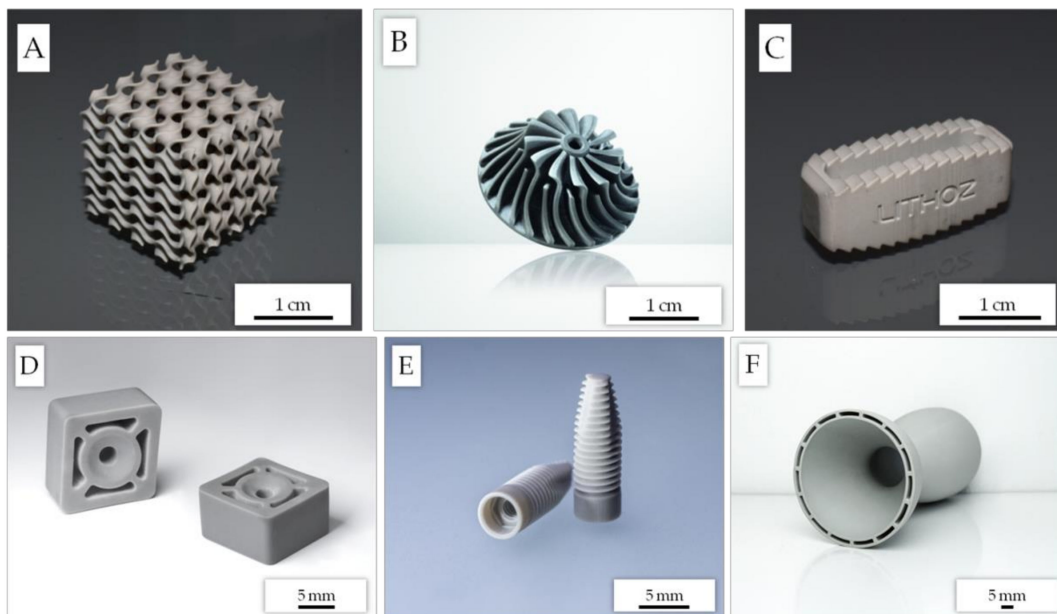


Figure 16. Printed and sintered silicon nitride-based ceramic demonstrators: (a) gyroids, (b) impeller and (c) spinal implant (posterior lumbar interbody fusion (PLIF) cage), (d) cutting tools, (e) dental two-piece implants with M1.6 inner thread and (f) de Laval nozzle.

Author Contributions: Printing, A.A.A. and T.P.; characterization, A.A.A., T.P. and T.K.; thermal post-processing, T.K.; writing—original draft preparation, A.A.A.; writing—review and editing, A.A.A., T.P., T.K. and M.S.; supervision, M.S.; project administration, M.S. All authors have read and agree to the published version of the manuscript.

Funding: This work was supported by the Austrian Research Promotion Agency (FFG) under the project number 859827 (AddiZwerk).

Acknowledgments: The authors thank Johannes Rauchenecker for the conduction of X-Ray diffraction analyses.

Conflicts of Interest: A.A.A., T.P. and M.S. are employees of the company Lithoz GmbH, supplier of the used LithaNit suspension and the CeraFab 3D printer. The authors declare no conflict of interest.

References

1. Riley, F.L. Silicon Nitride and Related Materials. *J. Am. Ceram. Soc.* **2000**, *83*, 245–265. [[CrossRef](#)]
2. Lee, M.R.; Russell, S.S.; Arden, J.W.; Pillinger, C.T. Nierite (Si₃N₄), a New Mineral from Ordinary and Enstatite Chondrites. *Meteoritics* **1995**, *30*, 387–398. [[CrossRef](#)]
3. Anonymous. *Brevier Technische Keramik*, 4th ed.; Fahner Verlag: Lauf, Germany, 2003.
4. Collins, J.F.; Gerby, R.W. New Refractory Uses for Silicon Nitride Reported. *J. Met.* **1955**, *7*, 612–615. [[CrossRef](#)]
5. Carle, V.; Schafer, U.; Taffner, U.; Predel, F.; Telle, R.; Petzow, G. Ceramography of High Performance Ceramics. *Prakt. Met.* **1991**, *28*, 359–377.
6. Pezzotti, G.; Oba, N.; Zhu, W.; Marin, E.; Rondinella, A.; Boschetto, F.; McEntire, B.; Yamamoto, K.; Bal, B.S. Human osteoblasts grow transitional Si/N apatite in quickly osteointegrated Si₃N₄ cervical insert. *Acta Biomater.* **2017**, *64*, 411–420. [[CrossRef](#)] [[PubMed](#)]
7. Webster, T.J.; Patel, A.A.; Rahaman, M.N.; Bal, B.S. Anti-infective and osteointegration properties of silicon nitride, poly (ether ether ketone), and titanium implants. *Acta Biomater.* **2012**, *8*, 4447–4454. [[CrossRef](#)]
8. Ishikawa, M.; de Mesy Bentley, K.L.; McEntire, B.J.; Bal, B.S.; Schwarz, E.M.; Xie, C. Surface topography of silicon nitride affects antimicrobial and osseointegrative properties of tibial implants in a murine model. *J. Biomed. Mater. Res. A* **2017**, *105*, 3413–3421. [[CrossRef](#)]
9. Bodišová, K.; Kašiarová, M.; Domanická, M.; Hnatko, M.; Lenčič, Z.; Varchulová Nováková, Z.; Vojtašák, J.; Gromošová, S.; Šajgalík, P. Porous silicon nitride ceramics designed for bone substitute applications. *Ceram. Int.* **2013**, *39*, 8355–8362. [[CrossRef](#)]
10. Springer, D.B.; Parvizi, J. *Periprosthetic Joint Infection of the Hip and Knee*; Springer: New York, NY, USA, 2014.
11. Krstic, Z.; Krstic, V.D. Silicon nitride: The new engineering material of the future. *J. Mater. Sci.* **2012**, *47*, 535–552. [[CrossRef](#)]
12. Hoffmann, M.J. High-Temperature Properties of Si₃N₄ Ceramics. *MRS Bull.* **2013**, *20*, 28–32. [[CrossRef](#)]
13. Hampshire, S.; Pomeroy, M.J. Viscosities of Oxynitride Glass and the Effects on High Temperature Behavior of Silicon Nitride-Based Ceramics. *Key Eng. Mat.* **2005**, *287*, 259–264. [[CrossRef](#)]
14. Martin, J.W. *Concise Encyclopedia of the Structure of Materials*; Elsevier: Amsterdam, The Netherlands, 2006.
15. ASTM. *Standard Terminology for Additive Manufacturing Technologies F2792 12*; ASTM International: West Conshohocken, PA, USA, 2012.
16. Moritz, T.; Maleksaeedi, S. Additive manufacturing of ceramic components. *Addit. Manuf.* **2018**, 105–161. [[CrossRef](#)]
17. Emanuel, M.; Haggerty, J.S.; Cima, M.J.; Williams, P.A. Three-Dimensional Printing Techniques. U.S. Patent 5,204,055, 20 April 1993.
18. Subramanian, K.; Vail, N.; Barlow, J.; Marcus, H. Selective laser sintering of alumina with polymer binders. *Rapid Prototyp. J.* **1995**, *1*, 24–35. [[CrossRef](#)]
19. Bertrand, P.; Bayle, F.; Combe, C.; Goeuriot, P.; Smurov, I. Ceramic components manufacturing by selective laser sintering. *Appl. Surf. Sci.* **2007**, *254*, 989–992. [[CrossRef](#)]
20. Bartolo, P.J.; Mitchell, G. Stereo-thermal-lithography: A new principle for rapid prototyping. *Rapid Prototyp. J.* **2003**, *9*, 150–156.
21. Das, A.; Madras, G.; Dasgupta, N.; Umarji, A.M. Binder removal studies in ceramic thick shapes made by laminated object manufacturing. *J. Eur. Ceram. Soc.* **2001**, *23*, 531–534. [[CrossRef](#)]
22. Cesarano, J.; Calvert, P.D. Freeforming Objects with Low-Binder Suspension. U.S. Patent 6,027,326, 22 February 2000.
23. Grida, I.; Evans, J.R.G. Extrusion freeforming of ceramics through fine nozzles. *J. Eur. Ceram. Soc.* **2003**, *23*, 629–635. [[CrossRef](#)]

24. Zocca, A.; Colombo, P.; Gomes, C.M.; Günster, J. Additive manufacturing of ceramics: Issues, potentialities and opportunities. *J. Am. Ceram. Soc.* **2015**, *98*, 1983–2001. [[CrossRef](#)]
25. Inamura, C.; Stern, M.; Lizardo, D.; Houk, P.; Oxman, N. Additive manufacturing of transparent glass structures. *3D Print. Addit. Manuf.* **2018**, *5*, 269–284. [[CrossRef](#)]
26. Griffith, M.L.; Halloran, J.W. Freeform Fabrication of Ceramics via Stereolithography. *J. Am. Ceram. Soc.* **1996**, *79*, 2601–2608. [[CrossRef](#)]
27. Bae, C.J.; Halloran, J.W. Integrally Cored Ceramic Mold Fabricated by Ceramic Stereolithography. *Int. J. Appl. Ceram. Technol.* **2011**, *8*, 1255–1262. [[CrossRef](#)]
28. Schatt, W. *Sintervorgaenge-Grundlagen*; VDI Verlag GmbH: Düsseldorf, Germany, 1992.
29. Pfaffinger, M.; Mitteramkogler, G.; Gmeiner, R.; Stampfl, J. Thermal debinding of ceramic-filled photopolymers. *Mater. Sci. Forum* **2015**, *825*, 75–81. [[CrossRef](#)]
30. Schwentenwein, M.; Homa, J. Additive Manufacturing of Dense Alumina Ceramics. *Int. J. Appl. Ceram. Technol.* **2015**, *12*, 1–7. [[CrossRef](#)]
31. Harrer, W.; Schwentenwein, M.; Lube, T.; Danzer, R. Fractography of zirconia-specimens made using additive manufacturing (LCM) technology. *J. Eur. Ceram. Soc.* **2017**, *37*, 4331–4338. [[CrossRef](#)]
32. Pfaffinger, M.; Hartmann, M.; Schwentenwein, M.; Stampfl, J. Stabilization of tricalcium phosphate slurries against sedimentation for stereolithographic additive manufacturing and influence on the final mechanical properties. *Int. J. Appl. Ceram. Technol.* **2017**, *14*, 499–506. [[CrossRef](#)]
33. Schmidt, J.; Altun, A.A.; Schwentenwein, M.; Colombo, P. Complex mullite structures fabricated via digital light processing of a preceramic polysiloxane with active alumina fillers. *J. Eur. Ceram. Soc.* **2019**, *39*, 1336–1343. [[CrossRef](#)]
34. Zanchetta, E.; Cattaldo, M.; Franchin, G.; Schwentenwein, M.; Homa, J.; Brusatin, G.; Colombo, P. Stereolithography of SiOC Ceramic Microcomponents. *Adv. Mater.* **2016**, *28*, 370–376. [[CrossRef](#)]
35. Koopmans, R.J.; Nandyala, V.R.; Pavesi, S.; Batonneau, Y.; Beauchet, R.; Maleix, C.; Schwentenwein, M.; Altun, A.A.; Scharleman, C. Comparison of HTP catalyst performance for different internal monolith structures. *Acta Astronaut.* **2019**, *164*, 106–111. [[CrossRef](#)]
36. Chung, K.; Nenov, N.S.; Park, S.; Park, S.; Bae, C.J. Design of Optimal Organic Materials System for Ceramic Suspension-Based Additive Manufacturing. *Adv. Eng. Mater.* **2019**, *21*, 1900445. [[CrossRef](#)]
37. Philipp, H.R. Optical properties of silicon nitride. *J. Electrochem. Soc.* **1973**, *120*, 295–300. [[CrossRef](#)]
38. Felzmann, R.; Gruber, S.; Mitteramkogler, G.; Tesavibul, P.; Boccaccini, A.R.; Liska, R.; Stampfl, J. Lithography-based additive manufacturing of cellular ceramic structures. *Adv. Eng. Mater.* **2012**, *14*, 1052–1058. [[CrossRef](#)]
39. Ekström, T.; Olsson, P.O.; Holmström, M. O'-sialon ceramics prepared by hot isotactic pressing. *J. Eur. Ceram. Soc.* **1993**, *12*, 165–176. [[CrossRef](#)]
40. Mitteramkogler, G.; Gmeiner, R.; Felzmann, R.; Gruber, S.; Hofstetter, C.; Stampfl, J.; Ebert, J.; Wachter, W.; Laubersheimer, J. Light Curing Strategies for Lithography-based Additive Manufacturing of Customized Ceramics. *Addit. Manuf.* **2014**, *1*, 110–118. [[CrossRef](#)]
41. Gibson, I.; Rosen, D.W.; Stucker, B. *Additive Manufacturing Technologies Rapid Prototyping to Direct Digital Manufacturing*; Springer: New York, NY, USA, 2010.
42. Fox, J.C.; Moylan, S.P.; Lane, B.M. Effect of process parameters on the surface roughness of overhanging structures in laser powder bed fusion additive manufacturing. *Procedia CIRP* **2016**, *45*, 131–134. [[CrossRef](#)]
43. Cother, N.E. Sialon ceramics—Their development and engineering applications. *Mater. Des.* **1987**, *8*, 2–9. [[CrossRef](#)]
44. Karageorgiou, V.; Kaplan, D. Porosity of 3D biomaterial scaffolds and osteogenesis. *Biomaterial* **2005**, *26*, 5474–5491. [[CrossRef](#)]

